Acta Materialia 265 (2024) 119612

Contents lists available at ScienceDirect

Acta Materialia

journal homepage: www.elsevier.com/locate/actamat

Full length article

Deciphering the structural heterogeneity behaviors of (K, Na)NbO_3-based piezoelectric ceramics with multi-scale analyses

Yafang Li [a], Anyang Cui [b,c,*], Kai Dai [a], Yuting Yan [a], Kai Jiang [a], Liyan Shang [a], Liangqing Zhu [a], Yawei Li [a], Jinzhong Zhang [a], Xiang Lv [d], Jiagang Wu [d], Zhigao Hu [a,e,*]

[a] Technical Center for Multifunctional Magneto-Optical Spectroscopy (Shanghai), Engineering Research Center of Nanophotonics & Advanced Instrument (Ministry of Education), Department of Physics, School of Physics and Electronic Science, East China Normal University, Shanghai 200241, China
[b] Key Laboratory of Optoelectronic Material and Device, Department of Physics, Shanghai Normal University, Shanghai 200234, China
[c] Chongqing Key Laboratory of Precision Optics, Chongqing Institute of East China Normal University, Chongqing 401120, China
[d] College of Materials Science and Engineering, Sichuan University, Chengdu 610065, China
[e] Collaborative Innovation Center of Extreme Optics, Shanxi University, Taiyuan, Shanxi 030006, China

ARTICLE INFO

Keywords:
(K, Na)NbO_3-based ceramic
Phonon dynamics
Structural heterogeneity
Phase boundary

ABSTRACT

Inducing local structural heterogeneity is one of the most attractive strategies to enhance the piezoelectricity in lead-free piezoceramics, while the underlying mechanisms have not been well clarified, such as phase coexistence and domain boundary. Here, we mainly focus on analyzing the structure evolution mechanism of $0.96(K_{0.48}Na_{0.52})(Nb_{1-x}Sb_x)O_3$-$0.04(Bi_{0.5}Ag_{0.5})ZrO_3$ ($0 \le x \le 0.1$) (KNN) lead-free piezoelectric ceramics to study the intrinsic structural contributions from chemical modifying and/or alloy replacement. We explore the relation between structural characteristics and physical functionality by combining macro-spectral and micro-heterogeneity characterizations. It was found that Raman- and infrared-active phonon evolutions with respect to the motion of oxygen octahedron reveal the enhanced lattice symmetry when x increases to 0.06, along with the upswing optical electronic transitions. Moreover, we clarify the local heterogeneous structure of ceramics in terms of the spatial distribution of phonon traits on the micron scale accompanied with the atom-resolution polar vector state. The detected nanoscale atomic displacement clusters are directly related to the excellent polarization properties. Additionally, the phonon thermodynamics evolution was investigated in a wide temperature range of 80-720 K with unpolarized and polarized geometries. The detailed phase transition evolution and rhombohedral–orthorhombic–tetragonal multi-phase coexistence have been confirmed with Sb incorporation. The present work boosts the understanding of the compound-structure-functionality relation of KNN-based heterophase coexistent system, which could promote the development of the promising high-performance piezoelectric materials.

1. Introduction

Potassium sodium niobate ($K_{0.5}Na_{0.5}NbO_3$, KNN) based material presents a rapid piezoelectricity enhancement in the last twenty years [1]. Accompanying with its ultrahigh recoverable energy storage density, promising biocompatibility, and satisfying piezo-catalytic activity, KNN-based system has been regarded as an advanced comprehensive functional material in the future applications [2–4]. However, the moderate performance and strong temperature dependence of polarization. properties are the formidable obstacles for KNN-based piezoelectric system [5]. Inspired of the significant d_{33} value with the orthorhombic–tetragonal (O–T) phase boundary by Saito et al. [6] many works have been focused on the exploration of composition-dependent phase boundary [7]. Recently, the emerging new phase boundary (NPB) has attracted much attentions due to its overwhelming d_{33} improvement and excellent temperature stability in KNN-based ceramics [8,9]. The essential trait of the ceramic with NPB is that the phase transition temperature points of rhombohedral–orthorhombic (T_{R-O}) and orthorhombic–tetragonal (T_{O-T}) can be simultaneously shifted to room temperature by chemical modification, which will construct the multi-phase coexistence of rhombohedral–orthorhombic–tetragonal (R–O–T) at commercial grade temperature. The R–O–T coexistence at NPB not only leads to the low polarization anisotropy, but also contributes to the easy polarization rotation of dipole, thereby further benefits for excellent piezoelectric properties [10]. In this regard, the crucial factor of NPB construction is to select the appropriate additives for KNN-based ceramic and tailor their content in the synthetic process.

* Corresponding authors.
E-mail addresses: aycui@phy.ecnu.edu.cn (A. Cui), zghu@ee.ecnu.edu.cn (Z. Hu).

https://doi.org/10.1016/j.actamat.2023.119612
Received 3 July 2023; Received in revised form 9 December 2023; Accepted 17 December 2023
Available online 22 December 2023

Among the investigated dopants in B-site from ABO_3 perovskite type, such as Ti, Zr, Hf, and Ta [11–14], the equivalent doping by Sb ions can concurrently decrease the T_{O-T} temperature and increase the T_{R-O} value at the superior shifting rates. It results from the stronger covalency between Sb 5*s* and O 2*p* orbital, which could stiffen the B-O network to inhibit the ferroelectric distortion and lead to a low energy barrier and flatten B cation potential slope [15]. Hence, Sb^{5+} cation is the most popular additive to achieve the NPB construction in most of B-site replacements. Actually, our previous report has also presented that the diffused phase with Sb doping can effectively contribute to a two-fold piezoelectric coefficient increase from 274 pC/N for $x = 0$ to 539 pC/N for $x = 0.05$–0.06 and a strain stability in a broad temperature range for KNN-based ceramic [16]. Nevertheless, the NPB behavior and structural variation have not still been clarified because only the main effects on piezoelectric properties from the doping have been presented.

While the realization of NPB may be the state-of-the-art method to acquire high piezoelectricity of KNN-based ceramics, the majority studies mainly focus on optimizing the physical performance so far. However, the doping effects on phonon dynamics and electronic transitions of KNN-based ceramics with NPB, which reflect the conformation of the molecule in its current state, have not been well investigated. In addition, the identification and distribution of crystalline phases, which play a guiding role in functional improving and material designing, have been rarely reported so far. In fact, the macroscopic and microscopic physical properties of single crystal or ceramic materials can be studied in depth by condensed matter spectroscopy. The direct method involves detecting variations in the lattice structure and electronic structure through photon energy or wavelength, thereby establishing a connection with the physical mechanism and understanding the intrinsic motivation. As we know, Raman scattering and infrared reflectance (IR) spectra are the nondestructive and complementary spectroscopic approaches to study the mesoscopic-scale structure and transformation process by analyzing the temperature or pressure dependencies of phonon anomalies and renormalization [17,18]. Particularly, Raman spectroscopy is a very sensitive tool to study the structural deformation of perovskites at a local scale, which not only can identify basic phase transformation but also detect subtle spectral alternations and reveal the underlying structural changes [19,20]. Furthermore, as a useful tool to obtain dielectric functions of material, spectroscopic ellipsometry (SE) can provide important insight on the electronic transitions with the effect of temperature and component. Therefore, how to connect the above condensed matter spectroscopy with the microstructural analysis and derive the reasonable phase characteristics and physical functionality could be one of the important issues. This is because the study will bridge the macro-spectral properties and micro-heterogeneity behaviors for KNN-based ceramics.

In this work, a NPB pattern with R–O–T multi-phase coexistence from $0.96(K_{0.48}Na_{0.52})Nb_{1-x}Sb_xO_3$-$0.04(Bi_{0.5}Ag_{0.5})ZrO_3$ ceramic has been successfully constructed by the Sb doping. We focus on elucidating the chemical effect on the lattice dynamics and temperature-driven coupling processes, as well as on the relation to the optimized physical properties. The Raman- and IR-active phonon modes have been identified with different Sb contents. Correspondingly, the enhanced structural symmetry and interband electronic transitions have been presented when x surpasses 0.06. Notably, the local structural heterogeneity were revealed by the spatial distribution of phonon characteristics and atom-resolution polar vectors, which give the extrinsic contribution of macroscopic performance. The inherent characteristics of Raman-active phonon frequency, linewidth, and depolarization ratio have systematically clarified the correlations between lattice vibration and phase transition by analyzing the thermal kinetics of BO_6 octahedra with unpolarized and polarized scattering geometries. This work would provide the primary evidences for understanding the physical correlation between the polycrystalline structure and macroscopic performance in KNN-based ceramics.

2. Materials and methods

2.1. The synthesis method of ceramics

$0.96(K_{0.48}Na_{0.52})(Nb_{1-x}Sb_x)O_3$-$0.04(Bi_{0.5}Ag_{0.5})ZrO_3$ ($KNNS_x$-BAZ, $x = 0$, 0.02, 0.04, 0.06, 0.08 and 0.10) ceramics were synthesized by the conventional solid-state reaction method. A certain stoichiometric ratio of K_2CO_3 (99%), Na_2CO_3 (99.8%), Nb_2O_5(99.5%), Sb_2O_3 (99.99%), Bi_2O_3 (99.999%), Ag_2O (99.7%) and ZrO_2 (99%) powders were mixed and then ground 24 h by ball-milled method. The homogeneous mixture was pre-sintered at 1123 K for 6 h in air. And then the powder was pressed into a disc of 10 mm diameter and 1 mm thickness under 10 MPa. Thereafter, the disc was sintered at 1323 K for 3 h and naturally cooled down to room temperature. The detailed preparation process could also be found in the previous reported [16]. Note that all the ceramics were double-polished before spectral measurements.

2.2. The microstructure characterizations and spectral measurements

The crystalline structures of $KNNS_x$-BAZ ceramics were determined by X-ray diffraction (XRD, Japan SmartLab), with a Cu-Kα radiation source. The surface morphology of ceramic is detected by atomic force microscopy (AFM, Dimension Icon, Brucker). The high-angle annular dark field scanning transmission electron microscopy (HAADF-STEM) specimen was prepared by the focused ion beam method (Nanolab Helios 650). The HAADF-STEM analyses were carried out on a double spherical aberration (Cs) corrected JEM-ARM300F microscope operated at 300 kV. The distribution of positional relationship between these atoms is determined using Calatom software. The STEM image was performed Gaussian filter for a Gatan digital micrograph to remove the zero-frequency and high-frequency noise above the information transfer limit. The initial coordinates of atoms were determined by threshold method of the filtered image. Qualified atomic regions are firstly selected manually and then the precise atom coordinates will be exported by multiple-ellipse fitting method [21]. Finally, the network of the vector relationships of the neighbor atoms will be expressed and after that the diagram of the polarization vector can be drawn out.

Raman spectra were collected on a micro-Raman spectrometer (Jobin-Yvon LabRAM HR 800 UV) in the frequency range of 80–1000 cm^{-1} with a 532 nm exciting laser. A Linkam THMSE 600 heating/cooling stage was equipped for the temperature-dependent Raman experiment in a wide temperature range of 80–720 K. Note that all scattering spectra are corrected by the Bose–Einstein temperature factor. The polarized Raman spectra were recorded upon parallel-polarized (VV) and cross-polarized (VH) scattering configurations. Raman mapping of ceramics was realized on a motorized *XY*-stage. The selected area of 5×5 μm consists of 34×34 pixels (1156 spectra).

The IR reflection spectra at the range of 80–1000 cm^{-1} were measured by a Bruker Vertex 80 V Fourier transform infrared spectrometer (Bruker Co., Billerica, MA) equipped with a 6-μm-thick mylar beam splitter, a DTGS detector, and a Hg lamp source. A gold mirror was adopted as a reference due to its absolute reflectance. The SE experiments were performed by near-infrared-ultraviolet optical ellipsometry (J. A. Woolam Co., Inc.) from 210 nm to 1350 nm with a spectral resolution of 5 nm. The incident angle was fixed at 70° incident angle.

3. Results and discussion

3.1. The anomalous phonon evolutions with new structural states

Fig. 1(a) shows the XRD patterns of $KNNS_x$-BAZ ceramics with different Sb content. No secondary phase was detected, indicating the homogeneous solid solution can be remained with Sb^{5+} doping [22]. Generally, the intensity ratio of $\{002\}_{pc}$ diffractions of perovskite subcell around $2\theta \approx 45°$ could identify the phase structure [23]. The

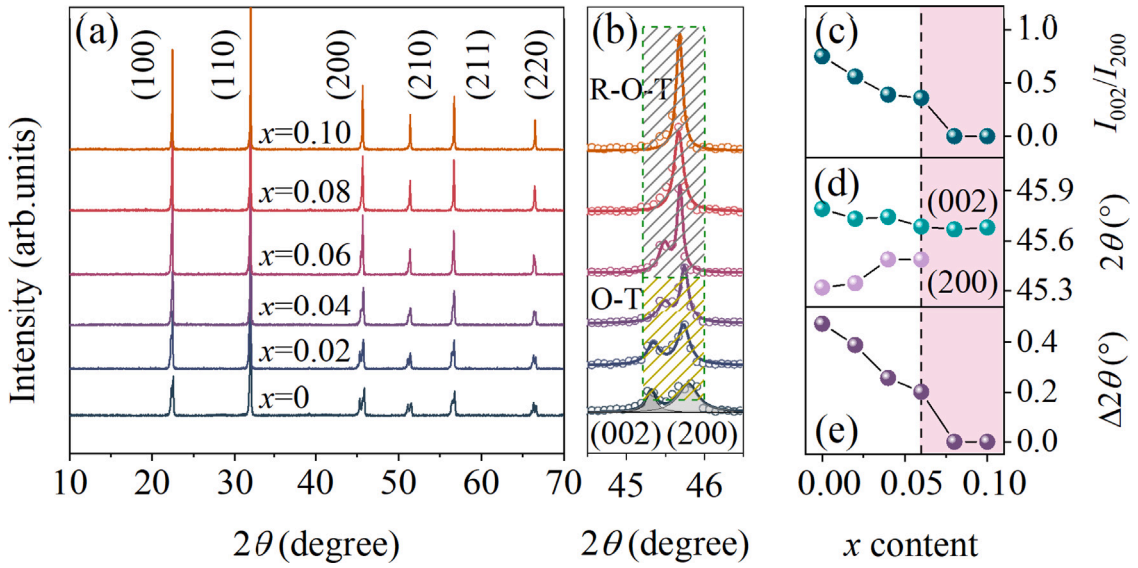

Fig. 1. (a) The XRD patterns of KNNS$_x$-BAZ ceramics with different Sb content. (b) The corresponding enlarged XRD patterns. Note that each spectrum is shifted in intensity for clarity. (c) The relative intensity ratio, (d) the peak position, and (e) the position difference of (002) and (200) diffraction peaks, respectively.

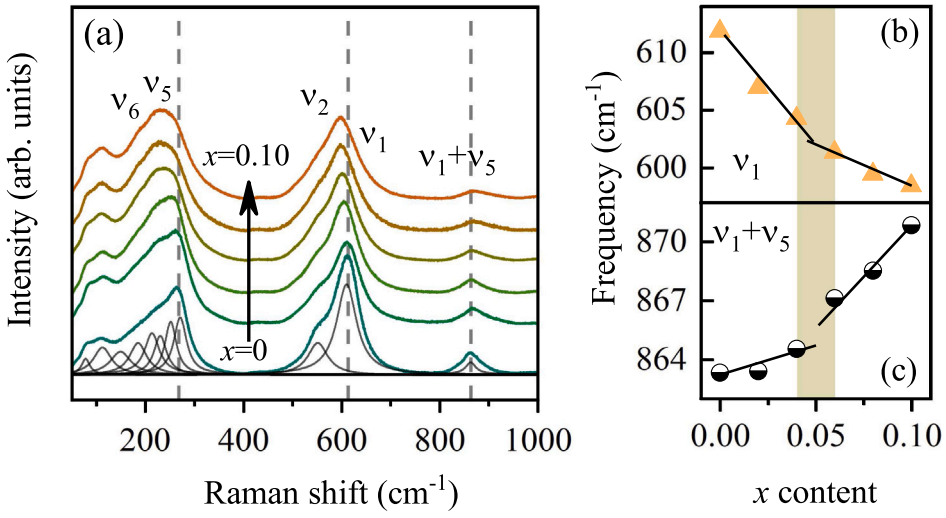

Fig. 2. (a) The Raman spectra of KNNS$_x$-BAZ ceramics with different Sb content at room temperature. The frequency variation trend of (b) ν_1 and (c) $\nu_1+\nu_5$ phonon modes with increasing the Sb content, respectively. (For interpretation of the references to color in this figure legend, the reader is referred to the web version of this article.)

enlarged patterns around 45° peaks have been well fitted in Fig. 1(b) and the related peak features were collected in Fig. 1(c–e). The relative intensity ratio $I_{(002)}/I_{(200)}$ from the ceramics with $x = 0$ is 0.75, which implies the O–T coexistence phase in this content. Thereafter, the ratio decreases to 0.36 when x increases to 0.06, indicating the more T phase content has generated. As the Sb content increases continuously, the ratio reduces to 0. In addition, two peaks of (002) and (200) shift toward each other and gradually merge into a single peak when the case of $x > 0.06$ appears in Fig. 1(d) and (e). The generated single peak represents the pseudo-cubic phase of KNNS$_x$-BAZ, which contains the diffused phase formed by R–O–T multi-phase coexistence [24]. Therefore, it can be concluded that the lattice structure of ceramics undergo a phase transition process of O–T ⟶ R–O–T with the Sb doping at room temperature.

Further investigation into the tiny distortion of the molecular structure and chemical bonds of KNNS$_x$-BAZ ceramics is imperative to comprehend the fundamental physical transformation process with chemical modifying. As shown in Fig. 2(a), the observed modes can be separated into external translational modes which relate to A-site cation (K^+, Na^+, Bi^{3+} and Ag^+) located mainly at the frequency less than 200 cm^{-1} and the internal vibrational modes of BO_6 octahedra located at the frequency range of 200–900 cm^{-1}, respectively. The BO_6 octahedra consists of six normal vibration $\Gamma = 1A_{1g}(\nu_1) + 1E_g(\nu_2) + 2F_{1u}(\nu_3, \nu_4) + F_{2g}(\nu_5) + F_{2u}(\nu_6)$, where $1A_{1g}(\nu_1) + 1E_g(\nu_2) + 2F_{1u}(\nu_3)$ represents stretching modes while the others are bending modes. The $\nu_1+\nu_5$ mode at about 860 cm^{-1} is attributed to the anharmonic coupling of ν_1 and ν_5 modes [20]. The evolution of lattice dynamics can be summarized by Raman- and IR-active phonon behavior in the following discussion.

Multi-Lorentzian oscillator functions were utilized to fit Raman spectra, as plotted in Fig. 2(a). The sharp modes at 150–300 cm^{-1} in the spectra of perovskite are regarded as a fingerprint for the occurrence of long-range polar order. The shoulder becomes broader which suggests the increment of short-range polarization. With increasing x value, the frequencies of ν_5 and ν_1 exhibit red shifts, while their scattering intensity gradually decreases. These are due to lattice mismatch caused by the smaller ionic radius ($R_{Sb^{5+}} = 0.61$ Å, $R_{Nb^{5+}} = 0.64$ Å) and the stronger electronegativity ($\chi_{Sb} = 2.05$, $\chi_{Nb} = 1.59$) of Sb^{5+} cation compared to the Nb^{5+} cation [25]. This tendency is due to the decrease in binding strength caused by the shortening of the distance between

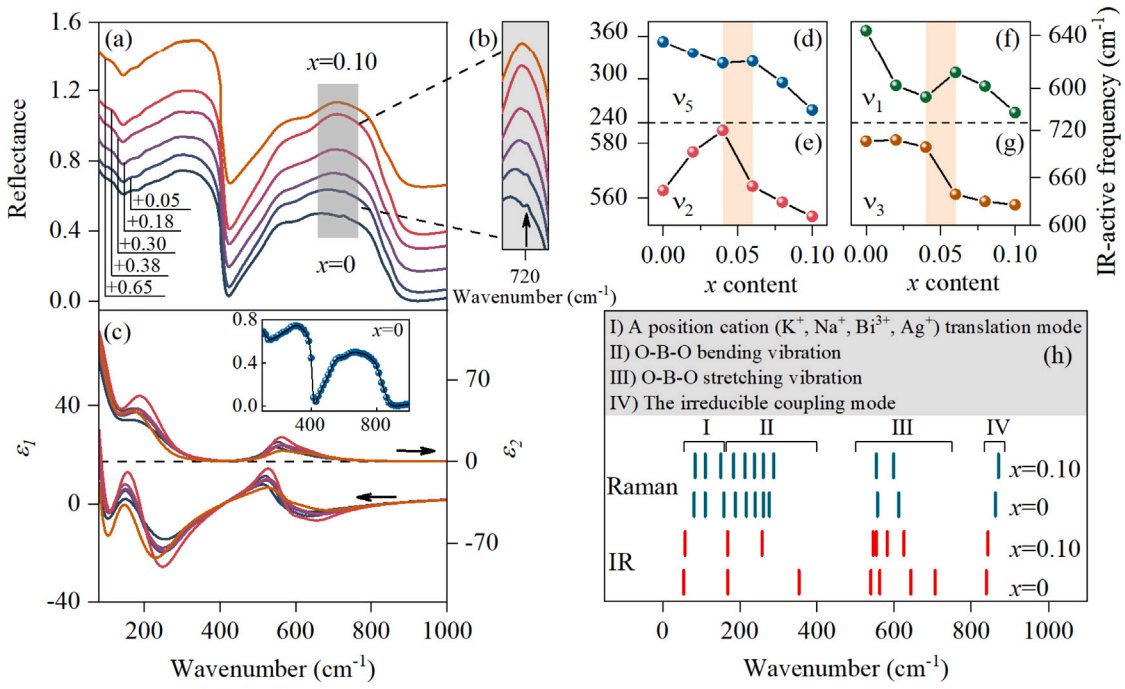

Fig. 3. (a) The IR spectra of $KNNS_x$-BAZ ceramics with different Sb content at room temperature. Note that some spectra are shifted in intensity for clarity and the shifted values are displayed at the left bottom. (b) The enlarged IR spectra in the range of 640–800 cm^{-1}. The arrow indicates the location of ν_3 phonon mode. (c) The real (ε_1) and imaginary (ε_2) parts of dielectric functions extracted by IR spectra. The inset displays the experimental (dotted) and the best fitting (line) spectra from the ceramic with x = 0. (d)–(g) Frequency variations of some typical IR-active phonons with increasing Sb content. (h) The comparison of Raman-active and IR-active vibration modes for the ceramics with x = 0 and 0.10, respectively.

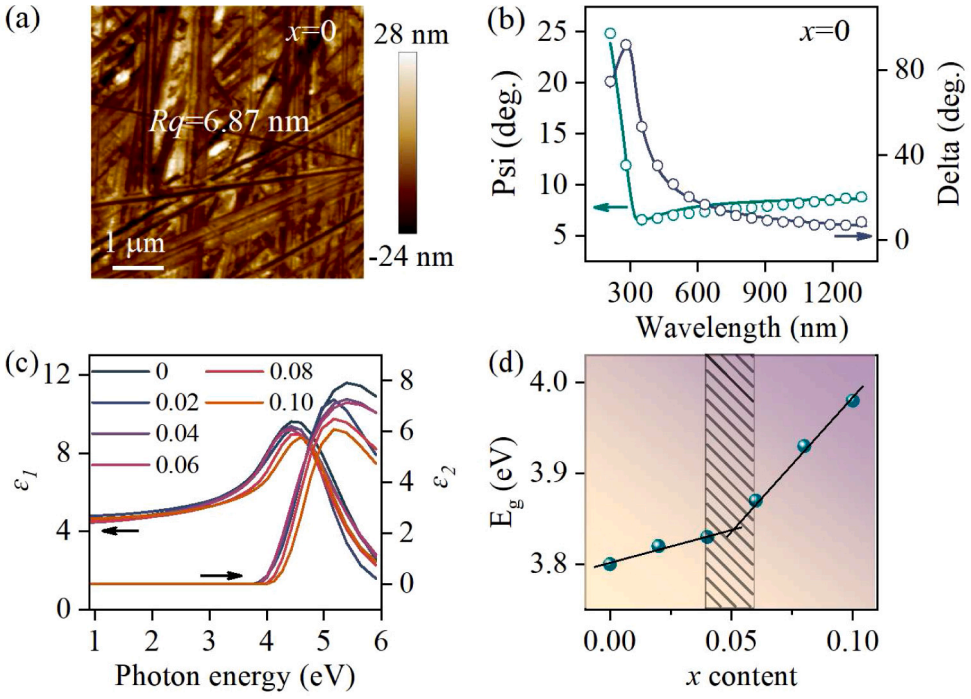

Fig. 4. (a) The roughness image from the ceramic with x = 0 by AFM measurement. (b) The experimental ellipsometric (dots) and the best fitting (solid lines) Psi (Ψ) and Delta (Δ) spectra from the ceramic with x = 0. (c) The derived real (ε_1) and imaginary (ε_2) parts of dielectric functions extracted by ellipsometric spectra. (d) The optical band gap (E_g) as a function of Sb content.

Nb^{5+} and its coordinated oxygen. Furthermore, the lower wavenumber of ν_1 mode signifies the weaker average polarizability of Nb ions and weaker distortion of NbO_6 units. The blue shift of $\nu_1+\nu_5$ mode can be associated to the different local possible superstructures from the random distribution of Sb^{5+} cation [26]. Both the evolution of ν_1 and $\nu_1+\nu_5$ modes indicate the gradual increased average crystal symmetry of KNN-based ceramics, which is consistent with XRD analysis. Note that both of the slope of ν_1 and $\nu_1+\nu_5$ frequency exhibit anomalous changes when x increases to 0.06, which would be a sign for the symmetry breaking and structural transformation to high-symmetry

ordered. Hence, the addition of Sb^{5+} would enhance the local covalency and induce local heterogeneity, which are responsible to the optimized piezoelectricity.

Fig. 3(a) displays the IR reflection spectra of $KNNS_x$-BAZ ceramics at room temperature. The reflectivity gradually increases in the low wavenumbers due to the possibility of dynamic disorder [27]. Noted that the stretching mode ν_3 of BO_6 octahedra which locates at around 720 cm^{-1}, can be distinguished in the enlarged IR spectra in Fig. 3(b). While the intensity of ν_3 gradually gets diminished and the peak position becomes undistinguishable with increasing x value. To further investigate the effect of Sb doping on the infrared dielectric functions and IR-active phonon frequency, IR spectra were fitted with the factorized oscillator model. Due to the small intensity of some modes from their accidental degeneracy, we only discerned 8 IR-active phonon modes of $KNNS_x$-BAZ ceramics. The well-fitted result of $x = 0$ sample is shown in the inset of Fig. 3(c). Furthermore, the dielectric functions can be obtained by Fresnel's formula [28]: $R = |\frac{\sqrt{\varepsilon}-1}{\sqrt{\varepsilon}+1}|^2$, R is the reflectivity. The real part (ε_1) and imaginary part (ε_2) of infrared dielectric functions of $KNNS_x$-BAZ are shown in Fig. 3(c). The ceramics tend to be transparent at the frequency region of 700–1000 cm^{-1}, since the ε_2 value is close to zero. In addition, compared with the dielectric functions of pure KNN ceramic in Buixaderas's report [27], the maximum ε_1 and ε_2 values shift toward lower frequency obviously, which result from the chaotic internal structure by the random distribution of A and B-site cations in $KNNS_x$-BAZ ceramic. Moreover, the variation trends of typical IR-active phonon frequency with Sb content are displayed in Fig. 3(d)–(g). The mode at 360 cm^{-1} can be ascribed to the B-O bending bonds in the octahedral vibrations, while the other modes at 560 cm^{-1}, 640 cm^{-1}, and 710 cm^{-1} are mainly caused by the octahedral stretching vibrations. The frequencies of four modes decrease as the Sb content increases, and their phonon frequency slopes exhibit noticeable shifts when x increases to 0.06. It indicates the remarkable rearrangement of lattice structure, which is also consistent with the Raman results. Based on the above analysis, the Raman and IR-active modes of $x = 0$ and 0.10 ceramics are summarized in Fig. 3(h) for comparison. The diagram clearly presents the origin of phonon modes and intuitively reflects the influence of Sb doping on lattice vibrational.

3.2. The abrupt variations from interband electronic transition and dielectric function at light frequency

Generally, the internal BO_6 octahedron of perovskite can determine its band structure and dominate the dielectric behavior. The variations of optical properties, such as reflectivity and dielectric constants, are related with the electronic band structure. Hence, the structural transition can be judged by the dielectric properties and electronic transition [29]. First, the roughness of ceramic with $x = 0$ is confirmed as 6.87 nm according to the AFM image in Fig. 4(a). A three-layer structure of air/surface rough layer/ceramic was constructed to evaluate the ellipsometric spectra. Note that the surface rough layer is cited by Brüggeman effective medium approximation [30], which contains 50% void component and 50% ceramic material. The dielectric function was determined by a single Tauc–Lorentz (T–L) oscillator dispersion relation, which can disclose the band gap (E_g) of ceramics. The T–L model can be expressed as $\varepsilon_1(E) = \varepsilon_\infty + \frac{2}{\pi} P\int_{E_g}^{\infty} \frac{\xi\varepsilon_2(\xi)}{\xi^2-E^2} d\xi$, $\varepsilon_2(E) = \frac{AE_nC(E-E_g)^2}{(E^2-E_n^2)^2+C^2E^2}\frac{1}{E}(E \geq E_g)$, $\varepsilon_2(E) = 0\ (E < E_g)$, where P refers to the Cauchy principal part of the integral, ε_∞ is the high frequency dielectric constant, and E is the incident photon energy. The parameter A, E_n, and C is the amplitude, peak position energy and broadening term of the T–L oscillator, respectively [31]. The best-fitting parameters are listed in Table 1 and the reasonable fitting result was shown in Fig. 4(b). Although the roughness difference between AFM and SE results appears, the phenomena could be reasonable due to the different detected regions and areas from the above macro and/or micro experimental techniques. The maximum value of ε_1 and ε_2 of $KNNS_x$-BAZ ceramics is located in the high-energy region in Fig. 4(c), which implies the evolution from transmission to absorption as photon energy enhances to the band gap. Both two parts of dielectric functions gradually decrease with increasing Sb content, which are influenced by the shrinkage of BO_6 structure after Sb^{5+} occupying part of Nb^{5+}. In addition, the band gap can be deduced from the non-absorbing region of spectra, which is shown as the model parameter E_g value in Table 1. For KNN crystal, the top bands of valence band maximum are derived from the hybridization of O-2*p* and Nb-4*p* orbits, while the bottom of conduction band minimum mainly consists of the Nb-4*p* orbits [32]. With the replacement of Sb^{5+}, the bottom of conduction bands will shift to higher energy states, leading to the enlargement of the band gap of ceramics. From Fig. 4(d), it can be seen that E_g remains on a moderate upward trend with low x content and then dramatically increases when the case of $x > 0.06$ appears. Hence, the anomalous variation of E_g demonstrates the variation of lattice structure from the phase transformation between $x = 0.04$ and 0.06 in $KNNS_x$-BAZ ceramics.

Table 1
The best-fitting parameters in the Tauc–Lorentz oscillator for SE at room temperature. Note that the error bars are also listed with parentheses.

Sample (x)	ε_∞	A	E_n (eV)	C (eV)	E_g (eV)	Roughness (nm)
0	1.21 (0.25)	314.99 (7.12)	4.73 (0.17)	2.26 (0.21)	3.80 (0.07)	9.23 (0.26)
0.02	2.38 (0.19)	238.97 (4.88)	4.72 (0.10)	1.58 (0.13)	3.82 (0.07)	5.31 (0.27)
0.04	1.42 (0.26)	358.75 (9.23)	4.50 (0.22)	2.22 (0.20)	3.83 (0.06)	7.46 (0.23)
0.06	1.19 (0.29)	407.05 (1.33)	4.35 (0.31)	2.32 (0.23)	3.87 (0.06)	7.60 (0.25)
0.08	2.17 (0.12)	290.98 (4.87)	4.63 (0.09)	1.65 (0.09)	3.93 (0.05)	11.27 (0.18)
0.10	2.67 (0.22)	234.58 (8.66)	4.78 (0.17)	1.51 (0.19)	3.98 (0.03)	13.28 (0.40)

3.3. Identification of local structural heterogeneity

Due to the fact that the numerous grain distribution and the intragranular stresses existed in grain boundaries, the phase transitions of piezoceramic are the gradual process, not as rapid as single crystals. Hence, some phases may be indiscernible when they diffuse into the majority phase element. Nevertheless, the changes of internal modes associated with BO_6 octahedron in heterophase could lead to the modification of Raman spectra. Therefore, the phase distribution can be guided by distinguishing phonon traits of BO_6 in a given material [33]. Moreover, the atomic-resolution polarization mapping of material can effectively identify polar nanoregions with multi-phase coexistence [34,35], which provides an absolute advantage in displaying the phase structure of relaxor ferroelectrics.

First of all, we study the phase coexistence of $x = 0$ ceramic at room temperature by micro-Raman imaging. Features from average scattering intensity ratio of I_{ν_2}/I_{ν_1} in Fig. 5(a) and Raman shift of ν_2 in Fig. 5(b) in the detected region were collected to obtain the Raman mapping images. The variations of these two features are reflected by the color intensity distribution in the selected region. Due to the intrinsic phase difference and the internal stress inhomogeneity, the mappings shows the obvious color partition and have the similar spatial distribution. From the color combination, three irregular regions can be observed and delimited with black dotted lines for clarity. As seen in Fig. 5(c–e), the corresponding Raman spectra at the range of 400–800 cm^{-1} from three typical points of A, B, and C in different

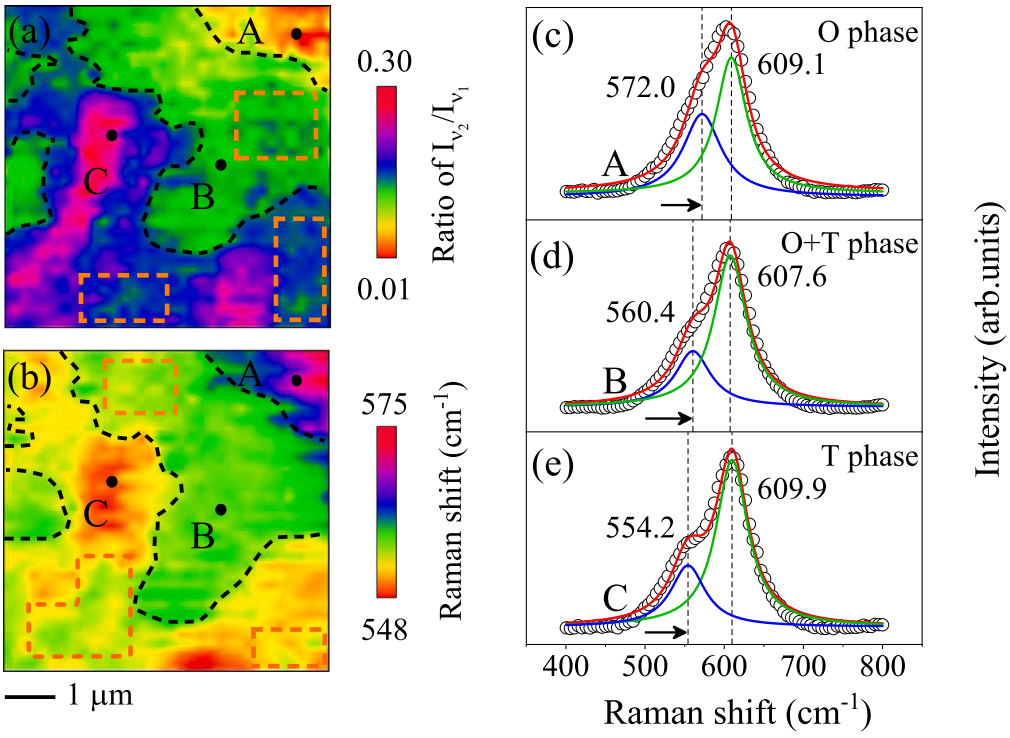

Fig. 5. The Raman mapping of $x = 0$ ceramic in a selected region. (a) The average Raman intensity ratio mapping of I_{v_2}/I_{v_1}. (b) The Raman frequency mapping of v_2 phonon mode. The black dashed lines sketch the separation boundary of different phase morphologies. The yellow dashed lines mark the irregular heterophase regions in the mappings. (c–e) The experimental Raman spectra (dots) and fitting results (red lines) in the range of 400–800 cm^{-1} corresponding to A, B, and C points in the left image, respectively. The positions of the blue and green peaks represent the location of v_2 and v_1 phonon, respectively. (For interpretation of the references to color in this figure legend, the reader is referred to the web version of this article.)

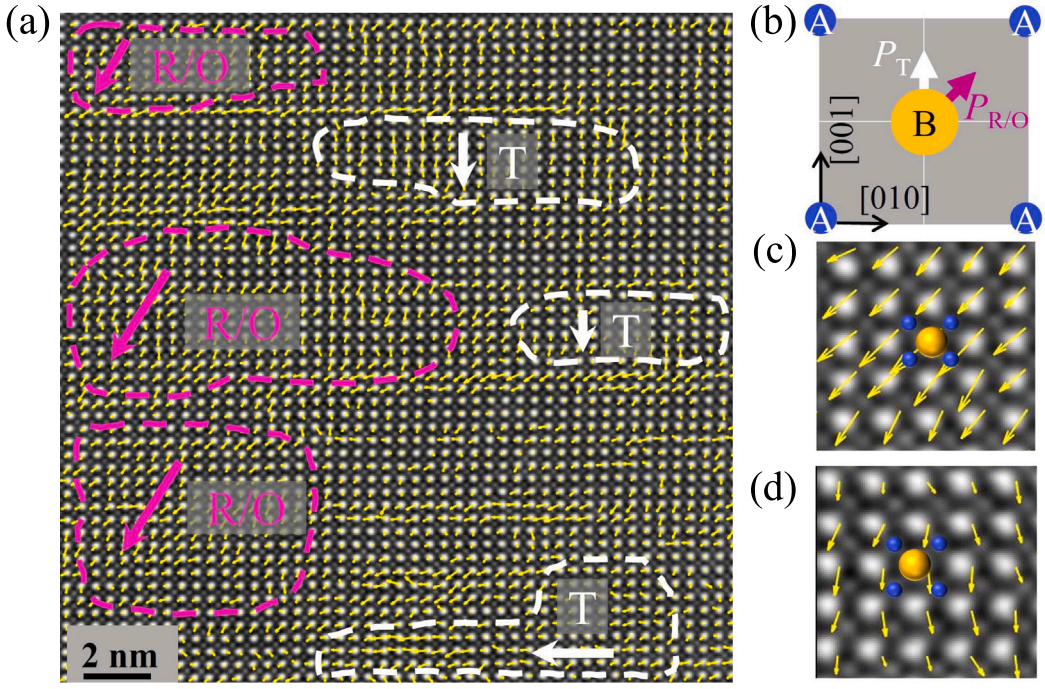

Fig. 6. Local symmetry and polarization mapping inside nanodomains from the ceramic with $x = 0.06$. (a) Atomically resolved HAADF-STEM image along ⟨100⟩ zone axes. The dashed lines delineate the nanodomains denoted by purple (R/O) and white (T) arrows. (b) The schematic project of the polarization vector along ⟨100⟩ zone axis, the T phase shows the vector along $(001)_{pc}$, while the R and O phases exhibit the vector along $(110)_{pc}$. (c–d) The magnified images of R/O phases and T phase region from (a) to show the cation displacements. (For interpretation of the references to color in this figure legend, the reader is referred to the web version of this article.)

regions are fitted with two Lorentzian peaks to explore the structural heterogeneity. An obvious red shift of v_2 phonon frequency from 572.0 to 554.2 cm^{-1} is relevant to the difference of polarization orientation in the selected area. According to the XRD results as mentioned in Part 3.1, the phase structure is confirmed as O-T phase coexistence for the ceramic with $x = 0$ in macroscopic. It has been reported that the

anti-symmetric ν_2 phonon mode will be magnified when the perovskite prone to orthorhombic phase, which is caused by the undermining of lattice symmetry. The frequency will be reduced when it tends to the tetragonal lattice. In addition, due to the symmetric characteristic of ν_1 mode, the frequency almost remains stable at ~609 cm^{-1} in three regions. Hence, three irregular areas can be divided into O phase, O-T phase, and T phase, respectively. Moreover, the phase distribution presents a dispersive multi-phase coexistence, such as the diffused regions in few tens nanometer size with yellow dashed lines in Fig. 5(a–b), instead of a clearly-defined and dense state in other study [33]. As a result, the occurrence of the structural heterogeneity provides a strong spectroscopic indication for the phase coexistence of ceramic and the phase of $x = 0$ ceramic has been distinguished from nanometer level to micron-level by Raman mapping measurement.

When the R phase diffuses in O–T phase, the ferroelectric state will form a slush nano-polar state with several nano-sized regions to minimize the domain-wall energy. This state provides lower polarization anisotropy, enabling easy polarization rotation and serves as the primary basis for acquiring high piezoelectric properties [36]. However, the laser spot diameter is ~1 μm in the Raman mapping experiment, which cannot detect the R–O–T nanoscale multi-phase coexistence in a higher resolution. Actually, the Raman mapping of $x = 0.06$ ceramic has also been detected in experiment. However, the results show the relative uniform distributions with few phonon intensity variations, which cannot distinguish phase distribution as Fig. 5. Hence, we carried out the HAADF-STEM image to clearly identify the phase structure and local symmetry of $KNNS_x$-BAZ composition of $x = 0.06$ ceramic. The domain structures are determined according to the projected displacement of B-site cation (the brighter spot) relative to its four nearest neighboring A-site cations (the darker spots), in which the atom displacement vectors are indicated by the yellow arrows in Fig. 6. The HAADF-STEM image is along ⟨100⟩ zone axis, which suggests that the polarization vector of T phase is along $(001)_{pc}$, while the vector of R/O phase is along $(110)_{pc}$, as shown in the schematic project in Fig. 6(b). According to the detailed polarization vectors among different phases in Fig. 6(c–d), we delineated the phase distribution with the purple dashed lines for R/O phase and the white dashed lines for T phase in Fig. 6(a). About 6–12 nm size atomic displacement clusters have been detected for the ceramic with $x = 0.06$. These clusters alternately arrange in the local structure and connect by the matrixes with weak displacement, which lead to the pseudo-cubic average structure for the case of $x = 0.06$. In addition, the presence of nanoscale clusters prone to easily switch by an external electric field, which make a strong extrinsic contribution for its promoted piezoelectric properties.

3.4. Anomalous temperature dependent behaviors from phonon modes

The phonon characteristics such as frequency, the full width of half maximum (FWHM), and recent concerned depolarization ratio of Raman spectra are the effective parameters to explore the first-order phase transition, lattice distortion, and molecular vibration geometry [19,20,37]. Next, the plentiful phase transition evolution and the precise transition points were distinguished by studying the phonon characteristics with the polarized and unpolarized scattering geometries. Fig. 7(a) gives the intuitive temperature-dependent Raman spectra intensity mapping from the ceramic with $x = 0$ in the range of 80–720 K. With increasing the temperature, the peak position of the main phonon modes present the red shift trend, while the phonon width are broadening. The overall ferroic distortion of $KNNS_x$-BAZ perovskite structure can be attributed to two main local distortions of the off-center shifts of B-site cations and BO_6 octahedral tilts. Thus, the temperature-dependent frequency and FWHM of ν_6 and ν_1 characteristic phonon modes, which are related to the lattice distortions, were further investigated to elucidate the composition dependence of the temperature-driven coupling process.

The perturbation model, which indicates the relationship between phonon frequency and temperature, can be expressed as: $\omega(T) = \omega_0 + \Delta\omega_E(T) + \Delta\omega_A(T)$, where ω_0 is the frequency at 0 K, $\Delta\omega_E(T)$ and $\Delta\omega_A(T)$ are the shift change by lattice thermal expansion and anharmonic coupling of phonon, respectively [38]. In addition, $\Delta\omega_E(T)$ is a negative value due to the volume expansion in the thermal process. According to the above formula, the frequency of phonon should exhibit a red shift with increasing temperature. Hence, the decreasing frequency between 80 K and 170 K in Fig. 7(b) can be reasonably attributed to thermal expansion of the lattice and anharmonic phonon–phonon interactions. However, the anomalous behaviors could be observed for ν_6 and ν_1 vibrational modes around the critical temperatures. For instance, the sudden blue-shift of ν_6 mode at 170 K cannot only be explained by the thermal effects, which is supposed to be a phase transformation in this temperature. With the heating process, the next anomalous shift in temperature-dependent frequency occurs at 420–430 K. The dashed line at 420 K exhibits the sudden changes of ν_1 and ν_6 frequency slopes. Another similar shift occurs at 600 K of ν_6 phonon modes, which implies another phase transformation at a higher temperature. Hence, the temperature of each phase transition for $x = 0$ can be acquired about 170 K, 420 K, and 600 K, respectively. Similarly, as shown in Fig. 7(d) and (f), the structural transition points from the case of $x = 0.06$ ceramic can be determined at 310 K and 470 K, and the transition points of $x = 0.10$ are 280 K and 350 K, respectively.

Furthermore, the corresponding FWHM of phonon modes are depicted in Fig. 7(c), (e) and (g). Temperature-dependent FWHM value can be expressed by $\Gamma(T) = \Gamma_0 + A[1 + n(\omega_1,T) + n(\omega_2,T)]$, where Γ_0 is the broadening of background derived from the disorder of lattice, A is the anharmonic coefficient, and $n(\omega,T)$ is the Bose–Einstein distribution function, which presents positive relation with temperature [39]. Hence, the value of FWHM will keep increasing in the heating process. However, the perturbation of the translational symmetry always occurs at the phase transition and generates the discontinuous tendency of FWHM. From Fig. 7(c), the increasing evolutions of ν_6 and ν_1 modes are ascribed to the anharmonic effect by temperature in the whole temperature region. However, the distinct deviations of slope in 170 K, 420 K, and 600 K indicate that three anharmonicities have occurred and are accompanied with the considerable phonon damping, which can originate from the significant structural transformations. Similarly, the transition temperature of other $KNNS_x$-BAZ ceramics also can be deduced by the FWHM evolutions (not shown). In addition, it is worth mentioning that the inset in Fig. 7(g) is the area proportion of ν_1 phonon mode after the area normalization of Raman spectra. The Area% value presents the abrupt change at the same temperature point with phonon frequency and FWHM evolutions. The evidence of phase transition, which is verified through the frequency shift, FWHM, and Area% in the heating process, is fundamentally related to the thermally induced symmetry rearrangement and the reassignment of the symmetry operation after the phase transition.

Note that the polarized Raman scattering have been regarded as the important method to elucidate the chemical effect on the crystal atomic dynamics with the temperature-driven coupling process. Especially, the depolarization ratio (ρ_l) from I_{VH}/I_{VV} in double cross-polarized geometries has been confirmed as the unique technique in determining the symmetry property of the vibrational mode, except for the phonon frequency and FWHM [20]. It can provide further information on the development of ferric long-range ordered domains [40]. It can be depicted by $\rho_l = \frac{3\beta^2}{45\bar{\alpha}+4\beta^2}$, where $\bar{\alpha}$ is the average value of molecular polarizability and β^2 is the degree of molecular anisotropy. In terms of the $KNNS_x$-BAZ polycrystalline ferroelectric, we can suppose that the region that Raman laser irradiated has m crystal grains with different orientations, and each of which contains n_i domains with the same polarization orientation. The total number of domains (N) in the irradiated area is expressed as: $N = n_1 + n_2 + \cdots + n_m$. Hence, the average value of molecular polarizability of polycrystal can be derived to: $\bar{\alpha}(\vec{\mu}) = \frac{1}{N}\sum_{i=1}^{m}\sum_{j=1}^{n_i}\alpha^{ij}(\vec{\mu})$. Since the different polarized

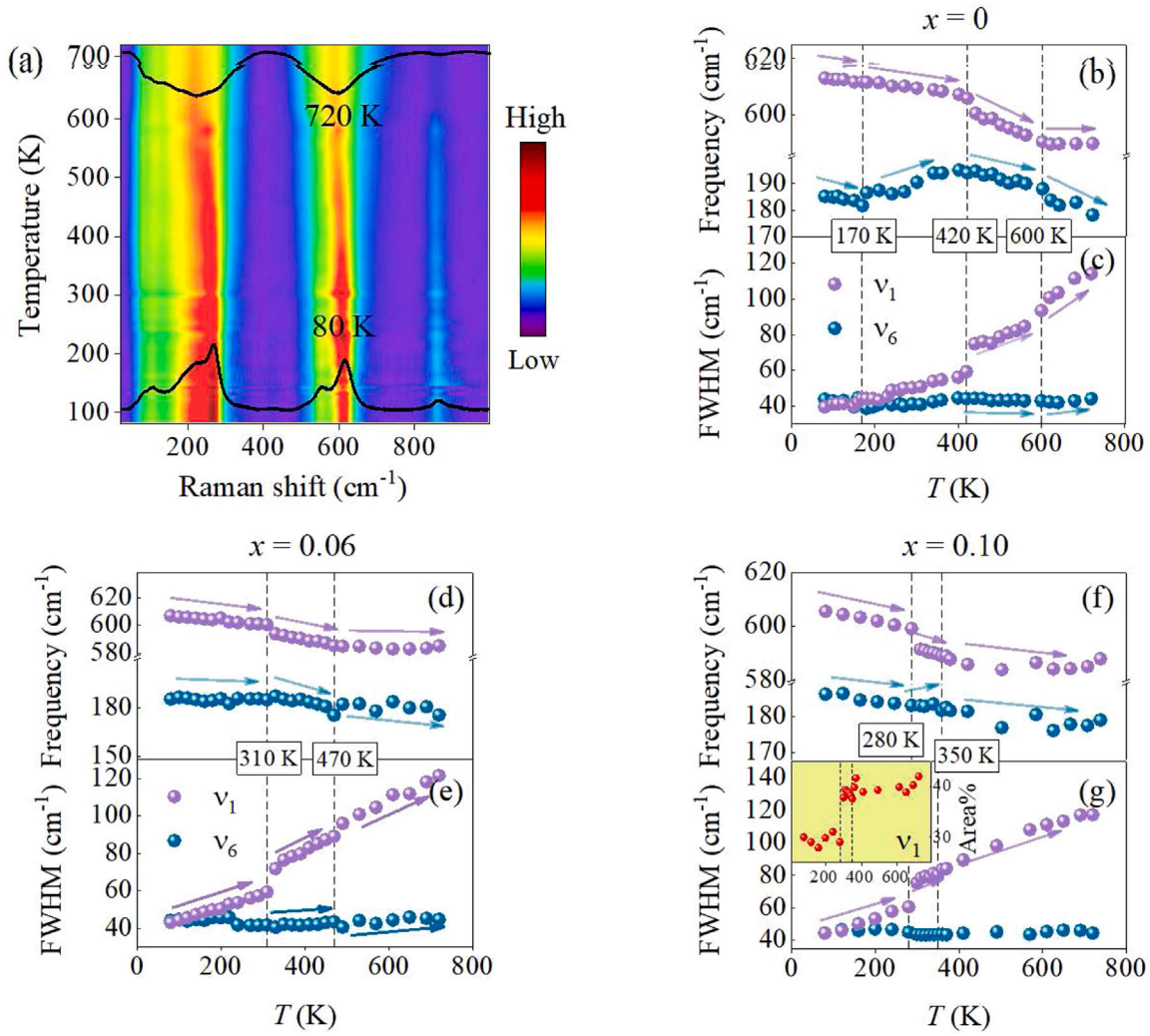

Fig. 7. (a) Temperature-dependent Raman scattering intensity mapping. Temperature-dependent phonon frequency and the corresponding FWHM evolutions of ν_1 and ν_6 vibration modes of the ceramics (b–c) $x = 0$, (d–e) $x = 0.06$, and (f–g) $x = 0.10$ from 80–720 K. The inset in (g) is the area proportion of ν_1 phonon mode after area normalization. The dashed lines indicate the temperature locations of anomalous phonon variation. (For interpretation of the references to color in this figure legend, the reader is referred to the web version of this article.)

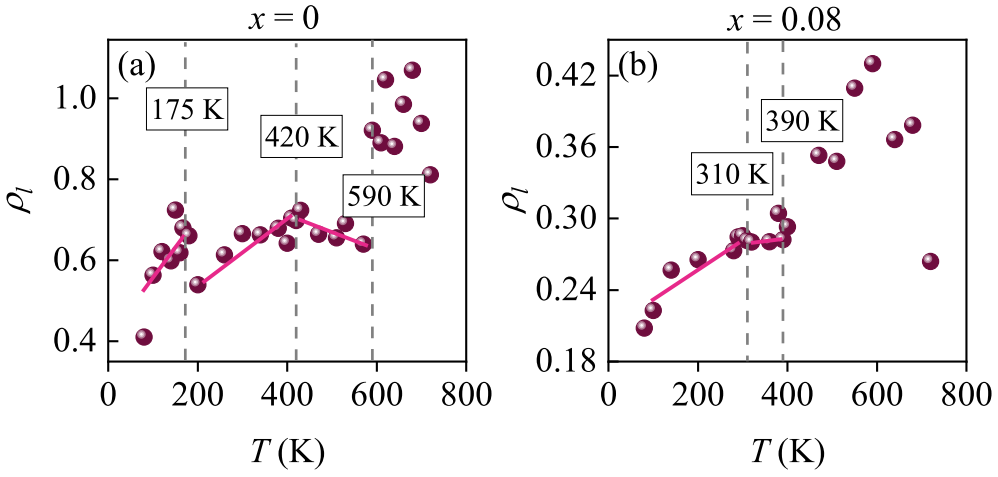

Fig. 8. Temperature-dependent depolarization ratio from the ceramics with (a) $x = 0$ and (b) $x = 0.08$ in regard to ν_1 phonon mode with the polarized Raman scattering, respectively.

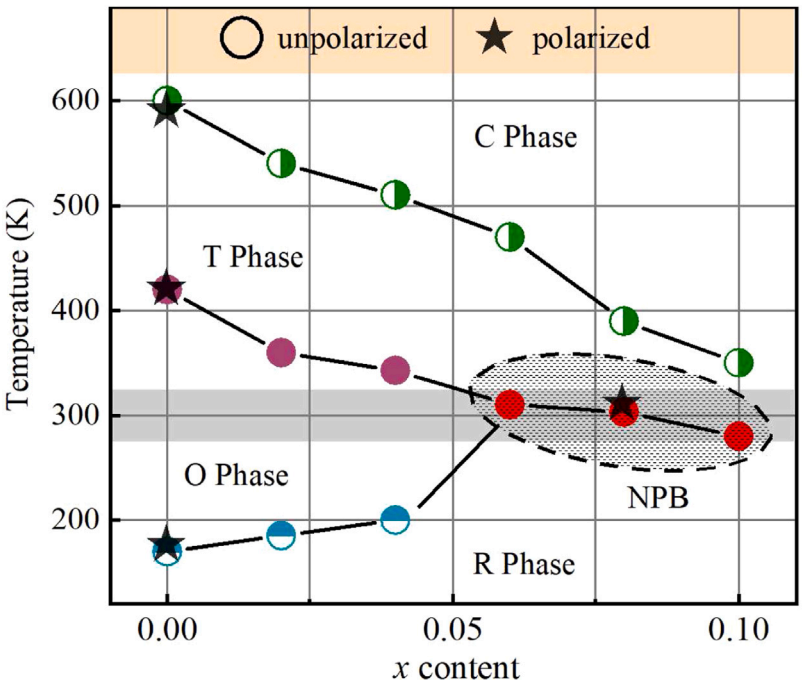

Fig. 9. Phase diagram of KNNS$_x$-BAZ ceramics with different Sb content. The phase transformation temperatures in the present work are marked with the symbols ○ for unpolarized and ★ for polarized Raman scattering results. The points in the shadow represent the phase transition temperatures with the new phase boundary.

variants of R phase along ⟨111⟩ zone axis, O phase along ⟨110⟩ zone axis, and T phase along ⟨001⟩ zone axis, the $\bar{\alpha}(\vec{\mu})$ must have disparity in the different ferroelectric phase coexistence for KNNS$_x$-BAZ ceramics. Therefore, the ρ_l of polycrystal could efficiently demonstrate the lattice symmetry evolution during the phase transition process. The variations of ρ_l value with the temperature from the ceramics with $x = 0$ and 0.08 were plotted in Fig. 8. The increased ρ_l values of two ceramics indicate that the deviation of the molecule from spherical to linear shape with increasing the temperature [41]. Hence, three discontinuous changes of the polarization state at 175 K, 430 K, and 590 K for the ceramic with $x = 0$, result from the occurrence of new polarized domains by phase transitions. In comparison, the symmetry-breaking temperature of the ceramic with $x = 0.08$ are confirmed as 310 K and 390 K, which are consistent with temperature-dependent unpolarized Raman spectra. It should be noted that when the temperature increases to Curie point, the high symmetry cubic phase will generate and lead to the broadening peaks from 200–800 cm^{-1}. In this case, modes will become overlapped and indistinguishable in our fitting process at high temperature, the fitting results of ν_1 phonon mode will be affected by other phonon modes and not be effectively separated. Hence, some unresolvable errors are generated in Fig. 8. Nevertheless, the ρ_l values significantly jump at Curie point and then maintain a certain level, which proves that the ρ_l of polycrystal could efficiently determine the phase transition and the lattice symmetry evolution by specifying the temperature dependence.

3.5. The phase transition ordering with phonon thermodynamics

Based on the deep analysis of the phonon characteristic including frequency, line width, and the depolarization ratio, the first-order phase transitions process of Sb doping KNNS$_x$-BAZ ceramics have been concluded in Fig. 9. As can be seen in the phase diagram, the incorporation of Sb in B-site presents a significant effect on the T_C, T_{O-T}, and T_{R-O}. Especially, the T_{O-T} and T_{R-O} completely converge to room temperature when x surpasses a certain degree of content, which implies the formation of NPB in KNNS$_x$-BAZ ceramic. The construction of NPB has been confirmed as the primary basis for acquiring high piezoelectric properties in niobate-based materials. On the one hand, the local heterogeneous structure has been confirmed by the spatial distribution of phonon traits and atom-resolution polar vector state. The nanoscale polarized clusters revealed by STEM image guarantee an easy polarization rotation, which contributes to a high piezoelectric coefficient in our previous study [16]. On the other hand, since the covalent bonding chance of Sb-O is close to 61%, which is larger than 43% from Nb-O [25], the increase of covalency of Sb element can stiffen the B-O network and inhibit the ferroelectric distortion [15]. In other words, the long-range ferroelectric ordering in KNNS$_x$-BAZ ceramics can be remained until x is beyond 0.06. Nevertheless, an increase in Sb content results in a contraction of the BO_6 octahedron due to the different ionic radii between Sb^{5+} and Nb^{5+}. The anomalous changes in phonon frequency and electronic transition can be attributed to the increased local stress fields, which further aggravate the short-range ferroelectric order and is responsible for the weak piezoelectricity of ceramics.

4. Conclusions

In this work, a new phase boundary with R–O–T multi-phase coexistence of $0.96(K_{0.48}Na_{0.52})(Nb_{1-x}Sb_x)O_3$-$0.04(Bi_{0.5}Ag_{0.5})ZrO_3$ piezoceramic was successfully constructed with Sb incorporation. We mainly focus on disclosing the structure evolution mechanisms of this compound-optimized lead-free ceramics by macro-spectral and microscopic structure techniques. We reveal that the chemical-modify induced oxygen octahedrons motion leads to anomalous Raman and IR-active phonon evolutions, accompanied with the sharp rise of optical E_g and dielectric function. In addition, the local heterogeneous structure of ceramic was identified in mesoscopic scale, according to the spatial distributions of average Raman intensity ratio of I_{ν_2}/I_{ν_1} and Raman shift of ν_2 phonon. The detected 6–12 nm size atomic displacement clusters revealed by atom-resolution polar vectors in microscopic dimension, are the direct evidence for excellent piezoelectric performance. Furthermore, the analysis of unpolarized and polarized

phonon thermodynamics give a macroscopic phase transition ordering. The present study would lead to clearly understanding of multi-scale structural properties of KNN-based ceramics, which is the physical origins of high-performance piezoelectricity.

Declaration of competing interest

The authors declare that they have no known competing financial interests or personal relationships that could have appeared to influence the work reported in this paper.

Acknowledgments

This work was financially supported by the National Natural Science Foundation of China (Grant Nos. 62090013, 61974043, 12104156, 62074058, and 61974044), the National Key Research and Development Program of China (Grants No. 2019YFB2203403), Projects of Science and Technology Commission of Shanghai Municipality, China (Grant Nos. 21JC1402100 and 23ZR1446400), Natural Science Foundation of Chongqing, China (CSTB2022NSCQ-MSX1367), the Program for Professor of Special Appointment (Eastern Scholar) at Shanghai Institutions of Higher Learning, China.

References

[1] Y. Saito, H. Takao, T. Tani, T. Nonoyama, K. Takatori, T. Homma, T. Nagaya, M. Nakamura, Lead-free piezoceramics, Nature 432 (2004) 84–87.
[2] L. Chen, S.Q. Deng, H. Liu, J. Wu, H. Qi, J. Chen, Giant energy-storage density with ultrahigh efficiency in lead-free relaxors via high-entropy design, Nature Commun. 13 (2022) 3089.
[3] M.H. Zhang, Q.H. Zhang, T.T. Yu, G. Li, H.C. Thong, L.Y. Peng, L.S. Liu, J. Ma, Y. Shen, Z.J. Shen, J. Daniels, L. Gu, B. Han, L.Q. Chen, J.F. Li, F. Li, K. Wang, Enhanced electric-field-induced strains in (K, Na)NbO_3 piezoelectrics from heterogeneous structures, Mater. Today 46 (2021) 44–53.
[4] J.Y. Liao, X. Lv, X.X. Sun, J.H. Li, H.M. Wang, Q. Chen, H.P. Lu, D. Wang, J. Bi, J.G. Wu, Boosting piezo-catalytic activity of KNN-based materials with phase boundary and defect engineering, Adv. Funct. Mater. (2023) 2303637.
[5] L. Egerton, D.M. Dillon, Piezoelectric and dielectric properties of ceramics in the system potassium-sodium niobate, J. Am. Ceram. Soc. 42 (1959) 438–442.
[6] W.F. Liu, X.B. Ren, Large piezoelectric effect in Pb-free ceramics, Phys. Rev. Lett. 103 (2009) 257602.
[7] L.M. Tan, X.C. Wang, W.J. Zhu, A.J. Li, Y.Y. Wang, Excellent piezoelectric performance of KNNS-based lead-free piezoelectric ceramics through powder pretreatment by hydrothermal method, J. Alloys Compd. 874 (2021) 159770.
[8] M. Waqar, H. Wu, J. Chen, K. Yao, J. Wang, Evolution from lead-based to lead-free piezoelectrics: engineering of lattices, domains, boundaries, and defects leading to giant response, Adv. Mater. 34 (2022) 21068455.
[9] J.Y. Liu, J.K. Shi, S.X. Xie, B. Wu, J.G. Zhu, Q.Y. Wang, Insight into the evolutions of microstructure and performance in bismuth ferrite modified potassium sodium niobate lead-free ceramics, Mater. Charact. 195 (2023) 112474.
[10] S. Gao, P. Li, J.W. Qu, W. Li, J.W. Zhai, F.F. Wang, J.G. Hao, P. Fu, Z.B. Pan, W.F. Bai, Crystallographic texture and phase structure induced excellent piezoelectric performance in KNN-based ceramics, J. Am. Ceram. Soc. 106 (2023) 3481–3490.
[11] C. Montero-Tavera, M.D. Durruthy-Rodríguez, F. D.Cortés-Vega, J.M. Yañez-Limón, Study of the structural, ferroelectric, dielectric, and pyroelectric properties of the $K_{0.5}Na_{0.5}NbO_3$ system doped with Li^+, La^{3+}, and Ti^{4+}, J. Adv. Ceram. 9 (2020) 329–338.
[12] T.A. Duong, F. Erkinov, M. Aripova, C.W. Ahn, B.W. Kim, H.S. Han, J.S. Lee, Ferroelectric-to-relaxor crossover in KNN-based lead-free piezoceramics, Ceram. Int. 47 (2021) 4925–4932.
[13] M. Dubernet, M.J. Pitcher, M. Zaghrioui, M. Bah, J. Bustillo, F. Giovannelli, I. Monot-Laffez, Synthesis routes for enhanced piezoelectric properties in spark plasma sintered Ta-doped KNN ceramics, J. Eur. Ceram. Soc. 42 (2022) 2188–2194.
[14] C. Wang, B.J. Fang, Y.H. Qu, Z.H. Chen, S. Zhang, J.N. Ding, Preparation of KNN based lead-free piezoelectric ceramics viacomposition designing and two-step sintering, J. Alloys Compd. 832 (2020) 153043.
[15] A. Villesuzanne, C. Elissalde, M. Pouchard, J. Ravez, New considerations on the role of covalency in ferroelectric niobates and tantalates, Eur. Phys. J. B 6 (1998) 307–312.
[16] N. Zhang, X. Lv, X.X. Zhang, A.Y. Cui, Z.G. Hu, J.G. Wu, Feasible way to achieve multifunctional (K, Na)NbO_3-based ceramics: controlling long-range ferroelectric ordering, ACS Appl. Mater. Interfaces 13 (2021) 60227–60240.
[17] M. Maczka, L. Macalik, J. Hanuza, Raman and IR spectra of the cation-deficient Aurivillius layered crystal $Bi_2W_2O_9$, J. Raman Spectrosc. 40 (2009) 2099–2103.
[18] K. Dai, A.Y. Cui, Y. Ye, K. Jiang, J.Z. Zhang, Y.W. Li, G.S. Wang, X.L. Dong, Z.G. Hu, J.H. Chu, Phase diagram with an antiferroelectric/ferroelectric phase boundary in $AgNbO_3$-$LiTaO_3$ energy-storage ceramics by lattice dynamics and electronic transitions, Phys. Rev. B 104 (2021) 174104.
[19] S. Klauer, M. Wohlecke, Local symmetry of hydrogen in cubic and tetragonal $SrTiO_3$ and $KTaO_3$: Li determined by polarized Raman scattering, Phys. Rev. Lett. 68 (1992) 3212.
[20] A.Y. Cui, Y. Ye, L.M. Zheng, K. Jiang, L.Q. Zhu, L.Y. Shang, Y.W. Li, Z.G. Hu, J.H. Chu, Exploring lattice symmetry evolution with discontinuous phase transition by Raman scattering criteria: The single-crystalline (K, Na)NbO_3 model system, Phys. Rev. B 100 (2019) 024102.
[21] Q. Zhang, C.H. Jin, H.T. Xu, L.Y. Zhang, X.B. Ren, Y. Ouyang, X.J. Wang, X.J. Yue, F. Lin, Multiple-ellipse fitting method to precisely measure the positions of atomic columns in a transmission electron microscope image, Micron 113 (2018) 99–104.
[22] Q. Liu, J.F. Li, L. Zhao, Y.C. Zhang, J. Gao, W. Sun, K. Wang, L.T. Li, Niobate-based lead-free piezoceramics: a diffused phase transition boundary leading to temperature-insensitive high piezoelectric voltage coefficients, J. Mater. Chem. C 6 (2018) 1116–1125.
[23] Q. Liu, Y.C. Zhang, L. Zhao, J. Gao, Z. Zhou, K. Wang, X.W. Zhang, L.T. Li, J.F. Li, Simultaneous enhancement of piezoelectricity and temperature stability in (K, Na)NbO_3-based lead-free piezoceramics by incorporating perovskite zirconates, J. Mater. Chem. C 6 (2018) 10618–10627.
[24] T. Wang, C. Wu, J. Xing, J.G. Wu, B.W. Li-Chen, X.Y. Xu, K. Wang, J.G. Zhu, Enhanced piezoelectricity and temperature stability in $LaFeO_3$-modified KNN-based lead-free ceramics, J. Am. Ceram. Soc. 102 (2019) 6126–6136.
[25] Y.C. Zhang, J.F. Li, Review of chemical modification on potassium sodium niobate lead-free piezoelectrics, J. Mater. Chem. C 7 (2019) 4284–4303.
[26] L. Luisman, A. Feteira, K. Reichmann, Weak-relaxor behaviour in Bi/Yb-doped $KNbO_3$ ceramics, Appl. Phys. Lett. 99 (2011) 192901.
[27] E. Buixaderas, D. Nuzhnyy, I. Gregora, S. Kamba, M. Berta, B. Malič, M. Kosec, Lattice dynamics and phase transitions in $KNbO_3$ and $K_{0.5}Na_{0.5}NbO_3$ ceramics, IEEE Trans. Sonics Ultrason. 56 (2009) 1843–1849.
[28] E. Buixaderas, D. Nuzhnyy, J. Petzelt, L. Jin, D. Damjanovic, Polar lattice vibrations and phase transition dynamics in $Pb(Zr_{1-x}Ti_x)O_3$, Phys. Rev. B 84 (2011) 184302.
[29] R. Singh, K. Kambale, A.R. Kulkarni, C.S. Harendranath, Structure composition correlation in KNN-BT ceramics-An X-ray diffraction and Raman spectroscopic investigation, Mater. Chem. Phys. 138 (2013) 905–908.
[30] D.A.G. Brüggeman, The calculation of various physical constants of heterogeneous substances. *I*. The dielectric constants and conductivities of mixtures composed of isotropic substances, Ann. Physics 416 (1935) 636–791.
[31] G.E. Jellison, F.A. Modine, Parameterization of the optical functions of amorphous materials in the interband region, Appl. Phys. Lett. 69 (1996) 371–373.
[32] C.W. Li, X. Xu, Q. Gao, Z.L. Lu, First-principle calculations of the effects of $CaZrO_3$-doped on the structure of KNN lead-free ceramics, Ceram. Int. 45 (2019) 11092–11098.
[33] F. Rubio-Marcos, A. Del Campo, J.F. Fernández, Resolution of the ferroelectric domains structure in (K, Na)NbO_3-based lead-free ceramics by confocal Raman microscopy, J. Appl. Phys. 113 (2013) 187215.
[34] H. Pan, F. Li, Y. Liu, Q.H. Zhang, M. Wang, S. Lan, Y.P. Zheng, J. Ma, L. Gu, Y. Shen, P. Yu, S.J. Zhang, L.Q. Chen, Y.H. Lin, C.W. Nan, Ultrahigh-energy density lead-free dielectric films via polymorphic nanodomain design, Science 365 (2019) 578–582.
[35] O. Paull, C.S. Xu, X. Cheng, Y.Y. Zhang, B. Xu, K.P. Kelley, A. de Marco, R.K. Vasudevan, L. Bellaiche, V. Nagarajan, D. Sando, Anisotropic epitaxial stabilization of a low-symmetry ferroelectric with enhanced electromechanical response, Nature Mater. 21 (2022) 74–80.
[36] J.F. Lin, G.L. Ge, J.F. Li, J. Qian, K. Zhu, Y.Q. Wei, C. Shi, G.H. Li, F. Yan, W.X. Li, J.L. Zhang, J.W. Zhai, H.J. Wu, Field-induced multiscale polarization configuration transitions of mesentropic lead-free piezoceramics achieving giant energy harvesting performance, Adv. Funct. Mater. 33 (2023) 2303965.
[37] J.F. Lin, Y.B. Cao, K. Zhu, F. Yan, C. Shi, H.R. Bai, G.L. Ge, J. Yang, W.W. Yang, Y.J. Shi, G.H. Li, H.R. Zeng, J.W. Zhai, Ultrahigh energy harvesting properties in temperature-insensitive eco-friendly high-performance KNN-based textured ceramics, J. Mater. Chem. A 10 (2022) 7978–7988.
[38] X. Huang, Y. Gao, T. Yang, W. Ren, H.M. Cheng, T. Lai, Quantitative analysis of temperature dependence of Raman shift of monolayer WS_2, Sci. Rep. 6 (2016) 32236.
[39] R. Cuscó, E. Alarcón-Lladó, J. Ibáñez, L. Artús, J. Jiménez, B.G. Wang, M.J. Callahan, Temperature dependence of Raman scattering in ZnO, Phys. Rev. B 75 (2007) 165202.
[40] N. Waeselmann, B. Mihailova, B.J. Maier, C. Paulmann, M. Gospodinov, V. Marinova, U. Biamayer, Local structural phenomena in pure and Ru-doped $0.9PbZn_1/3Nb_{2/3}O_3$-$0.1PbTiO_3$ near the morphotropic phase boundary as revealed by Raman spectroscopy, Phys. Rev. B 83 (2011) 214104.
[41] C. Banwell, E. McCash, Fundamentals of Molecular Spectroscopy, McGraw-Hill, New York, 1994.